

## A MULTISCALE FRAMEWORK FOR CHARACTERIZATION AND MODELING DUCTILE FRACTURE IN HETEROGENEOUS ALUMINUM ALLOYS

SOMNATH GHOSH\*, D. M. VALIVETI, CHAO HU and JIE BAI

*Mechanical Engineering, The Ohio State University,  
Scott Laboratory, 201 West 19th Avenue, Columbus,  
OH 43210, USA  
\*ghosh.5@osu.edu*

This paper develops three components contributing to the overall framework of multiscale modeling of ductile fracture in aluminum alloys. The first module is morphology-based domain partitioning (MDP) as a pre-processor to the multiscale modeling. This module delineates regions of statistical homogeneity and inhomogeneity with a systematic three-step process that is based on geometric features of morphology. The second module is detailed micromechanical analysis of particle fragmentation and matrix cracking of heterogeneous microstructures. A locally enriched VCFEM or LE-VCFEM is developed to incorporate ductile failure through matrix cracking in the form of void growth and coalescence using nonlocal Gurson–Tvergaard–Needleman (GTN) model. The third module develops a homogenized anisotropic plasticity-damage model in the form of GTN model for macroscopic analysis. Parameters in this GTN model are calibrated from results of homogenization of microstructural variables obtained from microstructural RVE. Numerical examples elucidate the strength of components of the overall framework.

*Keywords:* Multiscale domain partitioning; Voronoi cell FEM; ductile failure; anisotropic GTN model; multiscale modeling.

### 1. Introduction

Metals and alloys like cast aluminum alloys used in automotive systems contain microstructural heterogeneities in the form of silicon particulates, intermetallics, precipitates and voids in the microstructure. Experimental studies on ductile failure in Refs. 1–5 have shown that morphological variations strongly affect microstructural damage nucleation due to particulate cracking and interfacial decohesion, as well as ductile damage growth by matrix rupture due to void growth and coalescence. Caceres *et al.*<sup>4,5</sup> have demonstrated that larger and longer particles are more prone to cracking and damage accumulation with higher dendrite arm spacing. It is important to incorporate features of the actual microstructural morphology for developing robust predictive capability of failure properties, such as strain to failure, ductility and fracture toughness. The predictive capability of computational models using simplified representation of microstructural morphology, e.g., unit cell

models,<sup>6,7</sup> are limited due to simplification of the local features that are critical to failure. Ghosh and coworkers have attempted to model realistic representation of microstructures with nonuniform dispersion of heterogeneities<sup>8–10</sup> by combining digital image processing with microstructure modeling. Their microstructure-based Voronoi cell finite element model or VCFEM has been shown to offer significant promise in analyzing failure propagation in heterogeneous microstructural regions.

Modeling structure–material interaction in damage and failure analysis requires consideration of large domains. Multiscale modeling using adaptive two-way (bottom–up and top–down) coupling<sup>11,12</sup> provides the necessary framework for selective microscale analysis in a limited region of an otherwise macroscopic computational domain. The multiscale models undergo domain partitioning based on the evolution of stresses, strains, and/or damage in the microstructure. An optimal domain partitioning can significantly enhance the efficiency of multiscale computational models by keeping the “zoomed-in” regions of intense micromechanical analysis to a minimum. However, in many heterogeneous materials containing nonuniform microstructural dispersions, the local morphology may warrant embedding pockets of microstructural regions in a homogenized domain, even prior to starting the analysis. This necessitates a multiscale characterization module as a pre-processor to a concurrent multiscale model, where it is prudent to partition the initial computational domain based on information of the underlying microstructure. This paper introduces three important ingredients of multiscale modeling of ductile failure in heterogeneous cast aluminum alloys. These include: (i) a multiscale characterization-based preprocessor for multiscale models; (ii) microstructural analysis module for ductile fracture; and (iii) a homogenization-based continuum damage model for ductile materials that can be used in macroscopic analysis modules. The effective coupling of these individual modules will be addressed in a future publication.

The morphology-based domain partitioning (MDP) preprocessor to multiscale modeling is intended for two reasons: (1) to determine microstructural RVE’s that can be used in the “bottom–up” homogenization for different regions in the computational domain; and (2) to identify those regions, where the morphology alone (e.g., regions of dense clustering) can cause a breakdown in the homogenization assumption. Embedded regions requiring microstructural analysis should then be coupled with complementary regions of homogenized macroscopic analysis. The MDP process developed in Refs. 13 and 14 is discussed in Sec. 2. The complex interaction between competing damage modes in the presence of nonuniformities at the microstructural scale makes failure analysis rather challenging. Various computational studies have been conducted for understanding the elastic–plastic deformation and damage behavior of discretely reinforced MMC’s and other materials.<sup>15,16</sup> Many of these studies focus on the initial stages of ductile failure and do not consider the effect of microstructural morphology on the evolution of ductile failure by void growth in the matrix and coalescence. Ghosh *et al.* have developed

the Voronoi cell finite element model (VCFEM) to simulate particle cracking and interfacial debonding-induced damage<sup>9,10</sup> in particle and fiber-reinforced composites with complex nonuniform microstructural morphology. In the present work, the VCFEM with particle fragmentation is extended to incorporate ductile failure through matrix cracking in the form of void growth and coalescence. A nonlocal Gurson–Tvergaard–Needleman (GTN) model<sup>17,18</sup> is implemented in a locally enriched VCFEM framework or LE-VCFEM for simulating ductile fracture. In LE-VCFEM, the stress-based hybrid VCFEM formulation is adaptively enriched in bands of localized plastic flow and void growth with displacement-based elements to accommodate strain softening behavior.

In the final part, a homogenization-based anisotropic continuum damage model for porous plastic materials is developed for macroscopic analysis of heterogeneous ductile materials. The macroscopic constitutive laws are obtained by the homogenization of variables obtained from micromechanics simulations. Various continuum constitutive models have been developed based on unit cell analyses of composite and porous microstructures.<sup>19–21</sup> Most of these models do not consider the complexity of real microstructures and damage interaction. In this paper, an anisotropic GTN type constitutive model is developed for macroscopic ductile damage analysis in nonuniform microstructures with dispersed particles. The model is based on homogenization of microstructural variables obtained by LE-VCFEM analysis of microstructural representative volume element (RVE). The three modules are discussed next.

## 2. Morphology-Based Domain Partitioning

The morphology-based domain partitioning (MDP) process in this study consists of three steps, executed in sequence. They are: (a) simulation of necessary high resolution microstructural information at all points of a computational domain from continuous low resolution images of the entire domain and few sample high resolution images; (b) quantitative characterization of the microstructure to create effective metrics that can relate microstructural features to critical material behavior of the heterogeneous materials; and (c) domain partitioning based on functions of microstructural descriptors. The MDP process delineates regions corresponding to different length scales.

### 2.1. Microstructure reconstruction

A necessary requirement of the MDP process<sup>13,14</sup> is that accurate information of the microstructural morphology, at least with respect to certain characterization functions, be available at all points of the computational domain. This can be a very challenging and time-consuming task, if the entire image has to be acquired by optical or scanning electron microscopy. A method of preparing a montage of a large number of high magnification microstructural images followed by image compression has been proposed in Ref. 22. However, this process of extracting

microstructural images at each individual point may be prohibitively exhaustive for large domains. Alternate statistical methods include simulated annealing<sup>23</sup> and random sequential packing algorithm.<sup>24</sup> All these methods have shortcomings with respect to convergence to the actual image.

Since it is almost impossible to experimentally obtain contiguous high resolution microscopic images at all points, it is desirable to simulate the local microstructure from micrographs extracted at a few selected locations in the domain. A typical low resolution image of a cast aluminum alloy A319 is shown in Fig. 1. The low resolution micrograph does not provide adequate information required for microstructural characterization and modeling. The microstructure reconstruction process generates corresponding high resolution images with delineation of the multiphase morphology.

The digital micrograph of Fig. 1 can be resolved into a grid of pixels, with each pixel belonging to a certain level in the grayscale hierarchy. For a region  $\Omega_{mic}$  in the micrograph, the grayscale level of each pixel at  $(x, y)$  is represented by an integer valued indicator function  $I^g(x, y)$  which can assume any integer value between 0 and 255 at each point of the micrograph. A magnified image of a small region of this micrograph is shown in Fig. 2(a). Magnification refers to the pixel size and hence a magnified image will have larger size of pixels with the same number of grayscale pixels as the original image. Resolution, on the other hand, corresponds to the number of pixels or pixel density in an image. The high resolution

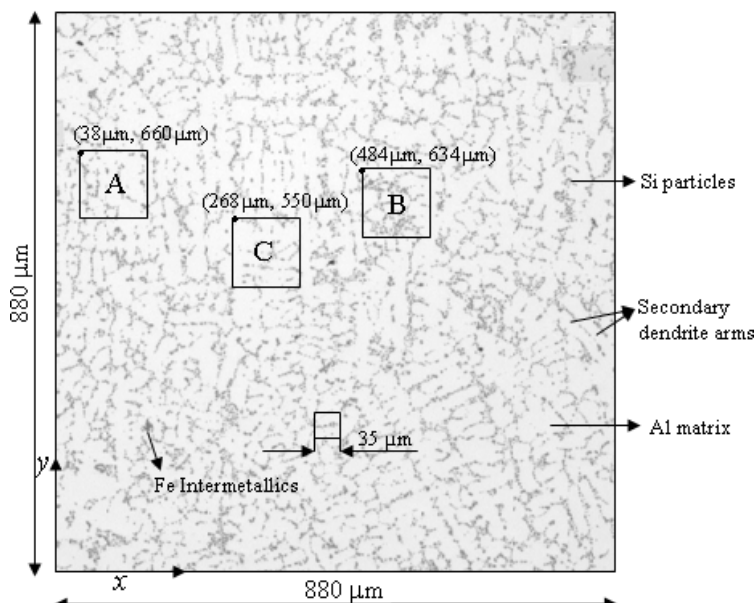


Fig. 1. Low magnification, low resolution digital image of cast aluminum alloy A319, for which high resolution micrograph of a window C is desirable with available high resolution micrographs at other locations A and B.

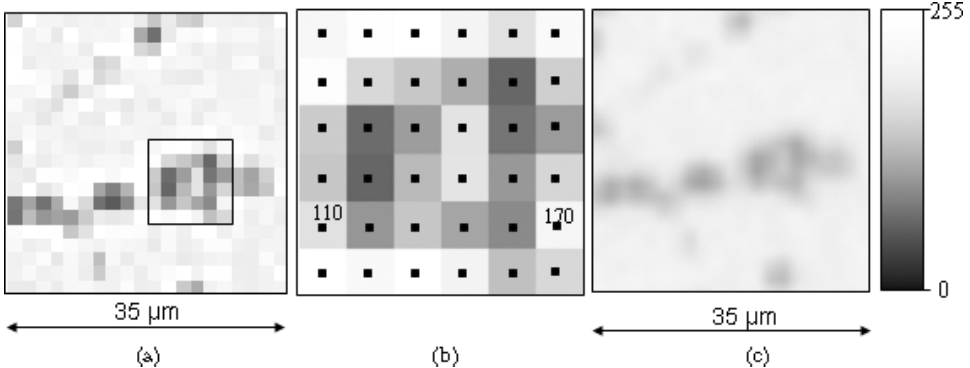


Fig. 2. High magnification  $35 \mu\text{m} \times 35 \mu\text{m}$  images of a region near  $C$ , shown in Fig. 1: (a) zoomed-in image showing larger pixels but with original resolution; (b) pixels of the square region marked in (a); and (c) a higher resolution micrograph of (a) obtained by interpolation.

microstructure reconstruction incorporates a wavelet interpolation with a gradient-based enhancement or *WIGE* method.

### 2.1.1. Wavelet-based interpolation in *WIGE* technique

In the WIGE image reconstruction technique, the integer indicator function  $I^g(x, y)$  is first interpolated in real space using a basis of wavelet functions. Let a window  $\Omega_w^{lrsm}$  of the low resolution image encompass a  $p \times q$  pixel grid. For a higher resolution image  $\Omega_w^{hrsm}$ , the same window may contain a  $p' \times q'$  pixel grid, where  $p' > p$  and  $q' > q$ . The grayscale level of each pixel in the  $p \times q$  pixel grid corresponds to the value of the indicator function  $I^g(x, y)$  at its centroid, which is thus represented by known discrete values at a set of equi-spaced points in the low resolution image window. This is shown in Fig. 2(b). Wavelet-based interpolation is used for estimating the indicator functions  $I_{wvlt}^g(x, y)$  in the high resolution pixel grid. Gaussian functions with continuous derivatives are popular wavelets bases<sup>25</sup> and can effectively represent sharp variations in image features. In encoding a  $p \times q$  pixel sub-region of a low resolution image, the indicator function may be expressed in terms of a level  $(m, k)$  Gaussian wavelet function as:

$$I_{wvlt}^{g'}(x, y) = \sum_{1 \leq n \leq p} \sum_{1 \leq l \leq q} \Phi_{m,n,k,l} = \sum_{1 \leq n \leq p} \sum_{1 \leq l \leq q} e^{-\frac{1}{2}(\frac{x-b_n}{a_m})^2} e^{-\frac{1}{2}(\frac{y-d_l}{c_k})^2} \beta_{m,n,k,l}. \quad (1)$$

Here  $(m, k)$  refer to the wavelet level in a multi-resolution wavelet representation and  $(n, l)$  correspond to the discrete translation of the bases in  $x$  and  $y$  directions, respectively. The parameters  $b_n, d_l$  correspond to translation, while  $a_m, c_k$  are dilation parameters. This yields a continuous interpolated image representation in terms of indicator function values of the low resolution image. The bases are

constructed by translation from one pixel to the next in the  $p \times q$  pixel subregion and the region is encoded with  $p \times q$  Gaussian functions. The wavelet coefficients  $\beta_{m,n,k,l}$  can be obtained by solving the matrix equation  $\{I^g\} = [F]\{B\}$  where  $\{I^g\}$ ,  $[F]$  and  $\{B\}$  are matrices of order  $pq \times 1$ ,  $pq \times pq$  and  $pq \times 1$ , respectively. The matrix  $\{I^g\}$  contains the values of the indicator functions from the available  $p \times q$  pixel data. The matrix  $[F]$  contains terms of Gaussian wavelet function, while the matrix  $\{B\}$  contains the unknown wavelet coefficients. Numerical studies have indicated that the values for which the system is stable are around  $p = 6$ ,  $q = 6$ .

The interpolation method is tested on the low resolution window marked A, in the A319 micrograph of Fig. 1. A high resolution SEM micrograph at the same location is shown in Fig. 3(a). The wavelet interpolated image on the  $480 \times 480$  pixel grid is depicted in Fig. 3(b). A pixel by pixel subtraction of  $I_{wvlt}^g(x, y)$  for image 3(b) from image 3(a) is depicted in Fig. 3(c). It is clear that interpolation alone is not sufficient for accurate high resolution microstructure, and subsequent image enhancement is essential.

### 2.1.2. Gradient-based post-interpolation enhancement

The enhancement method is developed to augment the wavelet interpolated micrographs with the aid of pixel data from high resolution calibrating images at a few different locations in the domain. The difference indicator function obtained above is expressed as:

$$I_{diff}^{g'}(x, y) = I_{hrs}^{g'}(x, y) - I_{wvlt}^{g'}(x, y). \quad (2)$$

The augmentation methodology requires the creation of a correlation function between  $I_{diff}^{g'}(x, y)$  and  $I_{wvlt}^{g'}(x, y)$  that will predict the high resolution image in  $\Omega_w^{hrs}$  from specific features of the interpolated image in  $\Omega_w^{intm}$ . For the interpolated

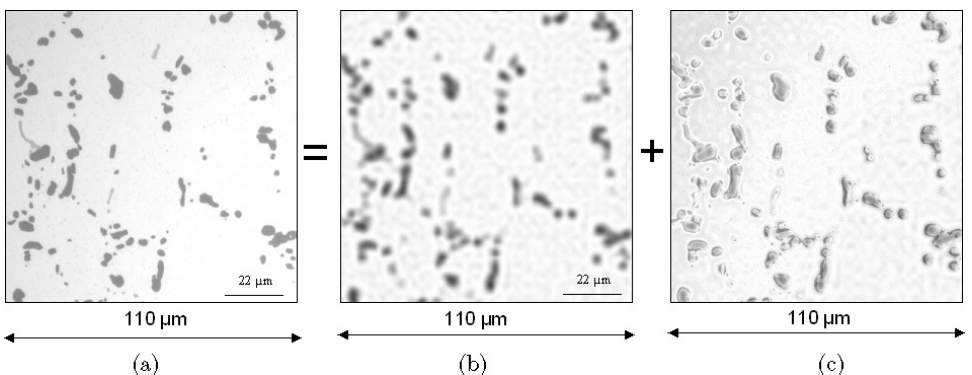


Fig. 3. High resolution micrographs at location A in Fig. 1: (a) actual high resolution micrograph; (b) micrograph obtained by wavelet-based interpolation in the WIGE algorithm; and (c) difference micrograph between (a) and (b).

image, the pixel-wise grayscale level or indicator function and its gradients are considered to be characteristic variables that adequately define the local phase distribution. A discrete correlation function is created between these characteristic variables of the interpolated image  $\Omega_w^{intm}$  and the indicator function value  $I_{diff}^{g'}(x, y)$  of the difference image  $\Omega_w^{diff}$  at locations where high resolution calibrating micrographs are available. This correlation is expressed in a functional form of the indicator function and its gradients as:

$$I_{diff}^{g'}(x, y) = P_{diff} \left( I_{wvlt}^{g'}(x, y), \frac{\partial I_{wvlt}^{g'}}{\partial x_+}, \frac{\partial I_{wvlt}^{g'}}{\partial x_-}, \frac{\partial I_{wvlt}^{g'}}{\partial y_+}, \frac{\partial I_{wvlt}^{g'}}{\partial y_-} \right). \quad (3)$$

Here  $P_{diff}$  corresponds to the most probable or expected value of the difference indicator function. The functional form of  $P_{diff}$  is not known *a priori*. Hence a discrete probability table is constructed from the calibration micrographs  $\Omega_w^{intm}$  and  $\Omega_w^{diff}$  to construct this correlation map. Each bin in the correlation map is represented by a range of values for each of the five variables and contains the values of the difference indicator function  $I_{diff}^{g'}$  belonging to the difference image  $\Omega_w^{diff}$ . The range of values to be assigned to each bin depends on the nature of variation of the variables. For example, the range  $0 \leq I_{wvlt}^{g'} \leq 255$  can be divided into as high as 256 bins or as low as 2 to 3 bins. However with increasing number of bins, the number of  $I_{diff}^{g'}$  entries in each bin will decrease and many of the bins may be empty for the calibration micrographs considered. Sparsity in the correlation bins renders the reliability of this probability table to be low. A moderate number of divisions ( $\sim 10\text{--}15$ ) is numerically found to be sufficient, as corroborated by convergence studies discussed later. The range of divisions for the gradients is selected such that they are able to distinguish between regions that belong to the interior and exterior of a given phase.

The location of high resolution calibrating micrographs in relation to the image being simulated is of considerable importance to the image augmentation process. A major assumption made is that if the calibrating micrographs contain the same constituent phases as the ones being simulated and if they are all produced by the same manufacturing process, the probability functions ( $P$ ) of local microstructural distributions will have a continuous variation from one micrograph to the next. The effect of the proximity between calibrating and simulated images can be addressed by assigning distance-based weights to the expected values in the probability table. Micrographs closer to the simulated image will have a stronger influence than those that are farther away. This dependence of a microstructure's correlation map on its spatial distance from each of the calibrating micrographs is represented by a “shape function” type interpolation relation, represented for two calibrating micrographs as:

$$I_{diff}^{g'}(x, y) = P_{diff}(x, y) = \left( \frac{1 - \xi}{2} \right) P_{diff}(x_A, y_A) + \left( \frac{1 + \xi}{2} \right) P_{diff}(x_B, y_B). \quad (4)$$

Here  $\xi = ((R_A - R_B)/R_{AB})$  and  $R_A$  and  $R_B$  are the distances of a pixel in the simulated image from the corresponding pixels in calibrating micrographs  $A$  and  $B$ , respectively, and  $R_{AB}$  is the distance between them. For microstructures containing a single predominant second-phase in the matrix, e.g., silicon for cast aluminum alloys, the different locations, e.g.,  $A$  and  $B$  may have statistically equivalent expected values of the probability. In this case, the effect of multiple locations in Eq. (4) will be minimal.

### 2.1.3. Validation test for WIGE algorithm

The effectiveness and convergence characteristics of the WIGE algorithm are tested by comparing characteristic metrics of the simulated microstructure with those for a real micrograph at the same location. The one-point, two-point and three-point statistics<sup>26</sup> are effective metrics for multiphase microstructure characterization and are used as validation tools. For the low resolution microstructural region of Fig. 1, windows at locations  $A$  and  $B$  are the high resolution calibration micrographs. The WIGE algorithm is used to simulate the image at a window  $C$ , for which a high resolution SEM micrograph is available for validation. The one-point probability function corresponds to the area fraction of the second phase particles. Its variation is plotted in Fig. 4(a) as a function of increasing number of divisions in the range of  $I_{wvlt}^{g'}$ , or bins in the probability table. The value at 0 bins corresponds to the micrograph with no enhancement. The simulated area fraction converges to the SEM image area fraction with about 10 discrete divisions or bins. The two-point probability function is defined as the probability of finding two points at the end of a line, separated by a distance  $r = (r_1 - r_2)$ , in the same phase of the microstructure. The % error in the two-point probability function between the actual and simulated images is defined as:

$$E_{\text{two-point}} = \frac{\sum_{r=0}^{r=L/2} |P_{ij}^{\text{SEM}} - P_{ij}^{\text{sim}}|}{\sum_{r=0}^{r=L/2} P_{ij}^{\text{SEM}}} * 100\%. \quad (5)$$

This error is evaluated along two orthogonal directions and is plotted in Fig. 4(b). Once again, a fast convergence is noted and the error stabilizes to a near zero value for around 10 bins. Similar convergence behavior is observed for the three-point probability function for three points at the vertices of an isosceles right triangle.

Convergence characteristics of the WIGE algorithm are quite satisfactory with respect to one-point, two-point and three-point correlation functions. Excellent agreement can be seen in the WIGE simulated microstructural image and the corresponding actual micrograph shown in Figs. 5(a) and 5(b). Thus, this method can be applied sequentially to all windows in the computational domain for obtaining high resolution images.

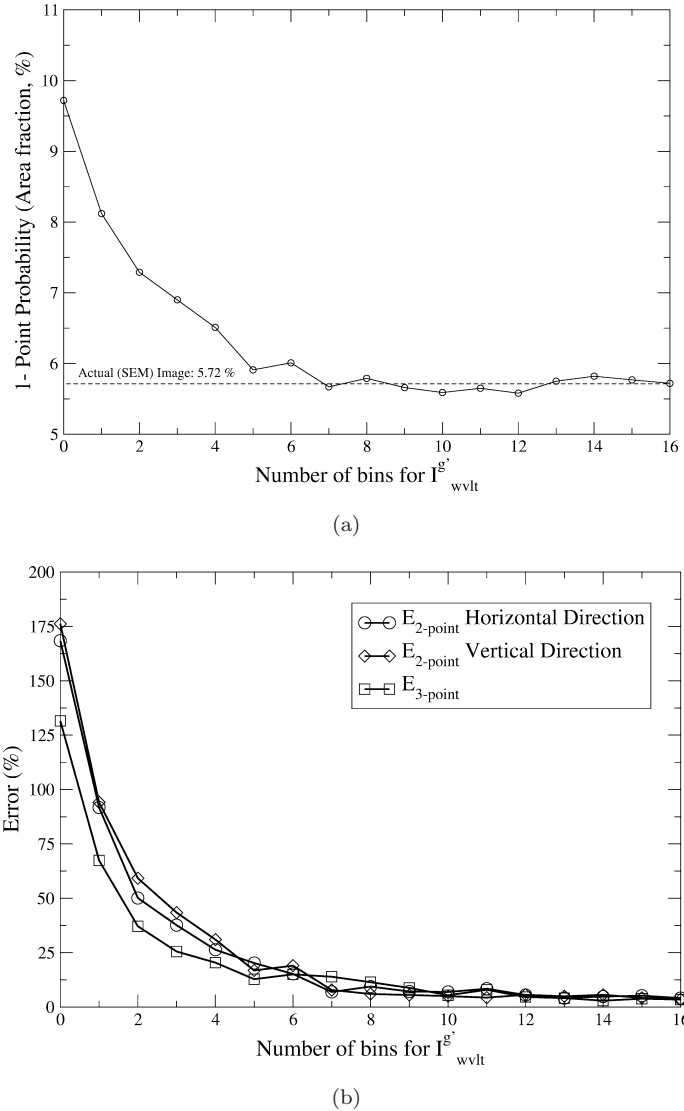


Fig. 4. Convergence plots for  $n$ -point statistics: (a) one-point probability function and (b) error in two-point and three-point probability functions.

## 2.2. Microstructure characterization

Damage in cast aluminum occurs by a combination of particle cracking, microcrack formation and growth in the matrix and coalescence of microcracks. Particle cracking depends on size, aspect ratio and the extent of clustering. Bigger particles inside a cluster show a higher propensity towards cracking. Numerous parameters have been used in the literature to quantify such features.<sup>1</sup> The following parameters are

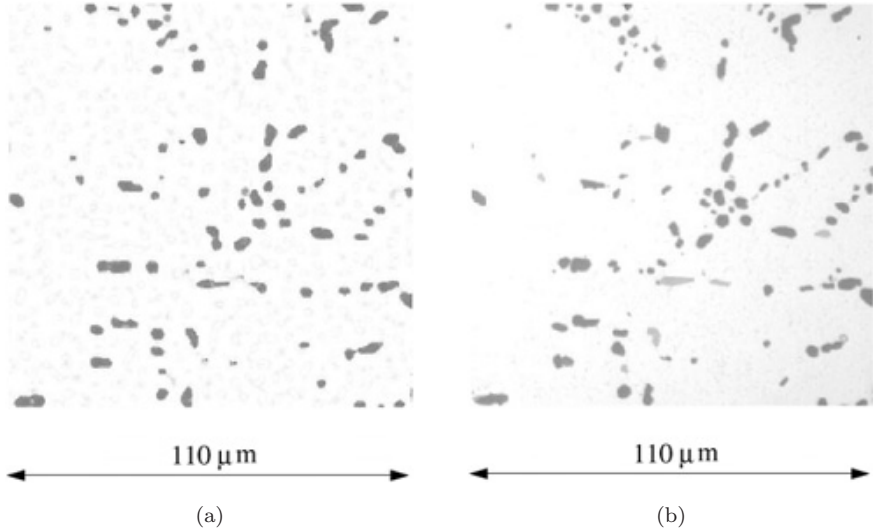


Fig. 5. High resolution micrographs at location  $C$  of Fig. 1 by the WIGE algorithm: (a) simulated micrograph by using the correlation table and (b) the real high resolution micrograph.

introduced in this work to quantify the size and distribution of particles:

- (a) Area fraction:  $A_f$  is measured as the ratio of total number of pixels belonging to heterogeneity to that of the entire microstructure.
- (b) Contour Index: Contour plots of parameters that represent local clustering are very helpful in identifying clusters. Such a contour plot can be generated for a microstructure with  $N$  inclusions using the characteristic radius  $R_{ch} = \sqrt{A_{image}/\pi N}$  as the field of influence for each heterogeneity. The total area of heterogeneities inside each characteristic circle is measured as contour intensity (COIN) at a point. The cluster contour index  $\iota$  is then defined in terms of the contour intensity as:

$$\iota = 1 - \frac{\text{Mean(COIN)}}{\text{Max(COIN)}}. \quad (6)$$

The mean and maximum values of COIN are evaluated from all points of the micrograph. A contour index  $\iota = 1.0$  denotes a cluster, while values closer to zero indicate uniform distribution. The contour index accounts for the area fraction of particles within a prescribed region.

### 2.3. Multiscale domain partitioning

Many heterogeneous materials have multiple length scales from morphological considerations. Local geometric features render some regions statistically inhomogenizable, i.e., statistical representative volume elements cannot be identified for these regions. Hence, in a true concurrent multiscale computational model,

these regions of geometric nonhomogeneity should be identified prior to analysis and concurrently modeled at the microstructural length scales. Once the high resolution microstructural features have been generated for all locations in the computational domain by the WIGE algorithm, the microstructural characterization functions and tools described above can be used for delineating regions with different scales. This section develops criteria that enables the pre-analysis partitioning of the computational domain into regions of homogeneity and inhomogeneity.

### 2.3.1. Statistical homogeneity and homogeneous length scale ( $L_H$ )

The  $n$ -point probability function  $S_n$  has been introduced in Ref. 26, which for a statistically homogeneous media satisfies the condition

$$S_n(x_1, x_2, \dots, x_n) = S_n(x_1 + \bar{x}, x_2 + \bar{x}, \dots, x_n + \bar{x}) = S_n(x_{12}, \dots, x_{1n}), \quad (7)$$

where  $x_1, x_2, \dots, x_n$  are position vectors of  $n$  points in the medium,  $\bar{x}$  corresponds to a fixed translation and  $x_{ij} = (x_j - x_i)$ . The one-point probability function  $S_1$  (the volume or area fraction) is a constant everywhere, i.e., homogeneity can be assumed at regions where  $S_1$  does not vary significantly. A homogeneous length scale  $L_H$  in the material microstructure is established in Ref. 27 from this consideration.  $L_H$  is the length scale above which the local variability in area fraction is smaller than a specified tolerance. It is evaluated in the following steps:

- (i) A large high resolution microstructural domain of characteristic dimension  $L$  is divided into finite squares, each of size  $D$ .
- (ii) The area fraction  $A_f$  of the heterogeneities in each square is evaluated. The ratio of standard deviation ( $\sigma_{A_f}$ ) to the mean area fraction ( $\mu_{A_f}$ ) is defined as the coefficient of variation or COV. This corresponds to the variation of  $A_f$  between the squares.
- (iii) Steps (i) and (ii) are repeated for different sizes  $D$ .
- (iv) For a Poisson distribution, the relation between the COV and the normalized square size  $D/L$  is derived in Ref. 27 as:

$$\text{COV}(A_f) = \frac{\sigma_{A_f}}{\mu_{A_f}} = \left( \frac{\pi}{4A_f} \right)^{0.5} \left( \frac{D}{L} \right)^{-1}. \quad (8)$$

The corresponding COV varies linearly with the normalized square size  $D/L$  in a logarithmic scale. The COV for cast aluminum alloy A319 microstructure is plotted as a function of  $D/L$  in Fig. 6.

- (v) The intercept of the plot with the  $D/L$  axis with a preset tolerance is evaluated. The corresponding size  $D$  is identified as the homogeneous length scale  $L_H$ .

Below this threshold  $L_H$ , it is necessary to change from a homogeneous to a heterogeneous domain representation with explicit delineation of heterogeneities.

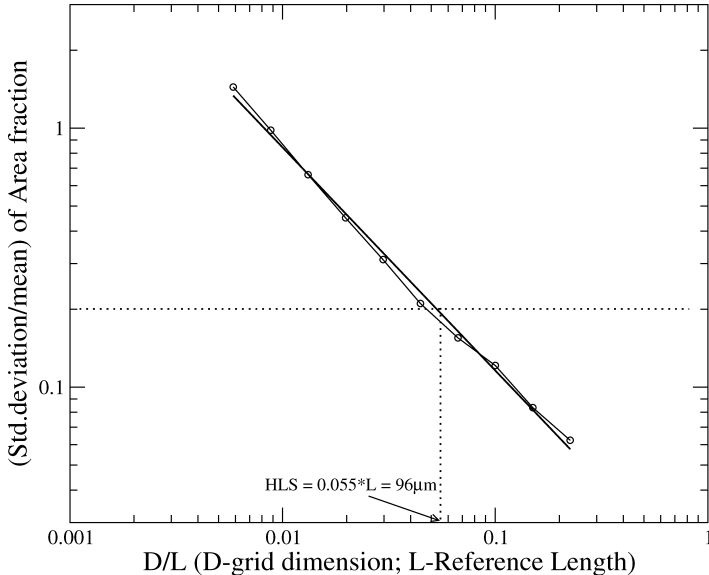


Fig. 6. Determination of homogeneous length scale  $L_H$  for aluminum alloy A319, using coefficient of variation of area fraction.

### 2.3.2. Domain partitioning criteria

The MDP process begins with a coarse discretization of  $\Omega_{comp}$  into  $N_p^0$  subdomains or partitions, as shown in Fig. 7(a). A microstructural unit is defined as a high resolution subhomogenization length scale microstructural region  $\Omega_{mic}$  of dimension  $\chi * L_H$  where  $\chi < 1$ . The factor is chosen as  $\chi = 0.5$  in this work. Any given subdomain  $i$  is assumed to be made up of  $M^i$  underlying microstructural units. Statistical functions representing the variation of a descriptor in the  $M^i$  microstructural units are evaluated for successive partitioning of a subdomain  $i$ . The area fraction  $A_f$  and contour index  $\iota$  are used to construct a refinement criterion function. It is constructed in terms of the mean parameters  $\mu(A_f)$  and  $\mu(\iota)$  for the  $M^i$  microstructural units within each subdomain  $i$ , and is expressed as  $F_i = \mu(A_f)\mu(\iota)$ . The refinement function is evaluated in each subdomain, together with those in each of its four divisions  $F_i(l)$ ,  $l = 1, \dots, 4$ . A subdomain  $i$  is partitioned if  $(F_i - F_i(l))/F_i > C_{f1}$  for any of the four subregions. The prescribed tolerance is  $C_{f2} = 0.10$  corresponding to 10% variation. The successive partitioning process reduces the subdomain size locally, and may ultimately reach the homogeneous scale limit  $L_H$ . Once  $L_H$  is reached, only one additional step of further partitioning is possible. The level below  $L_H$  is not homogenizable and hence cannot be refined any further. A special criterion is required for this partitioning. Each of the subsequent partitions contains only one microstructural unit  $M^{loc}$  of dimension  $0.5 * L_H$ . It is not possible to evaluate the statistical functions for a single  $M^{loc}$ . The criterion is constructed in terms of the variation of average local area fraction  $A_f$ . Partitioning below  $L_H$  is

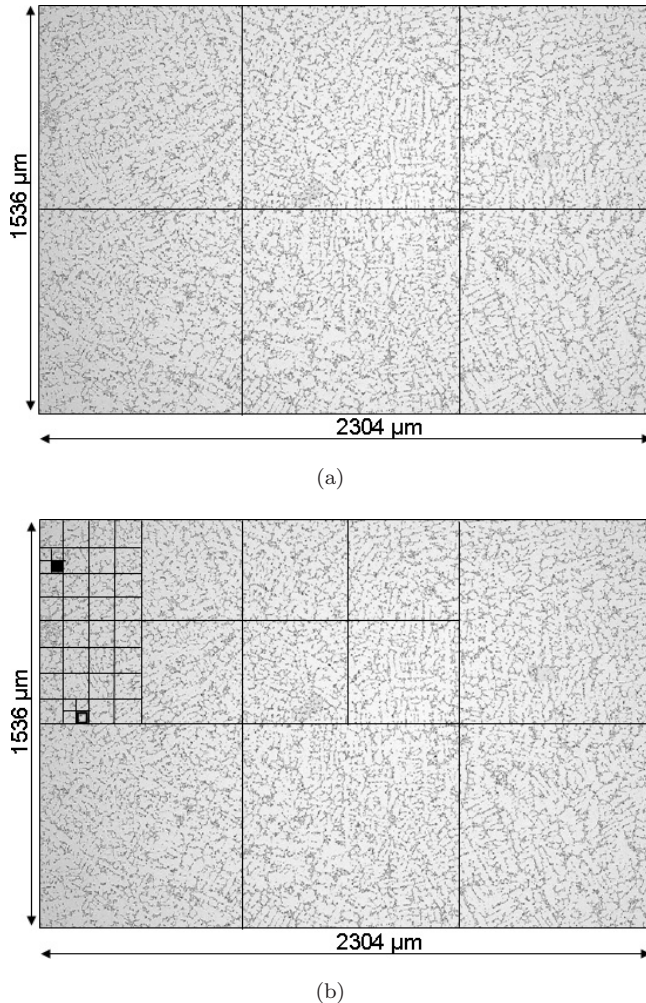


Fig. 7. (a) Microstructural image of cast aluminum alloy A319 to be partitioned and (b) result of the MDP process. Regions in dark boxes are inhomogeneous and need to be analyzed with micromechanical model.

governed by the criterion

$$\left( \frac{(A_f)_i}{(A_f)_\Omega} \right) \left( \frac{(A_f)_i - (A_f)_i(l)}{(A_f)_i} \right) > C_{f2},$$

where the first term corresponds to the local area fraction of subdomain  $i$  with respect to that of the entire domain and the second term corresponds to the difference in local area fraction and its four subdivisions. Any subdomain below the  $L_H$  threshold is characterized by significant variation in the local area fraction. Consequently those partitions for which the variation is really large are classified as inhomogeneous and opened up for explicit microstructural representation

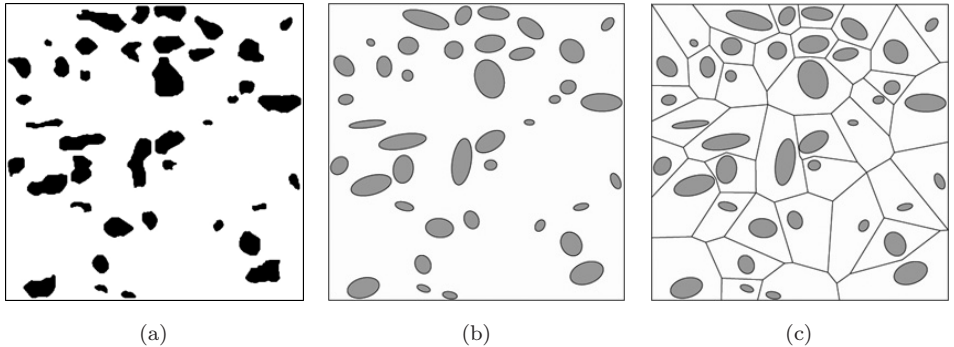


Fig. 8. (a) Micrograph at region marked in Fig. 6(b); (b) equivalent microstructure with elliptical particles and (c) Voronoi cell FEM mesh of the equivalent microstructure.

in the multilevel model. The factor  $C_{f2}$  is taken as 0.75, corresponding to a 75% difference in the critical regions of the microstructure. The combined microstructure simulation-characterization-partitioning method delineates the hierarchy of scales in the computational model as demonstrated in the following example.

#### 2.4. Numerical example

The morphology-based domain partitioning (MDP) methodology is applied to the microstructures of cast aluminum alloy A319 with secondary dendrite arm spacing of  $23\ \mu\text{m}$ . The low resolution computational micrograph  $\Omega_{comp}$  of dimensions  $2304\ \mu\text{m} \times 1536\ \mu\text{m}$  is shown in Fig. 7(a). The WIGE algorithm generates high resolution images of all points in  $\Omega_{comp}$  by constructing a correlation table, from two  $110\ \mu\text{m} \times 110\ \mu\text{m}$  high resolution SEM image windows. The locations of these two windows are shown as *A* and *B* in Fig. 1. The homogenization length scale is evaluated using a tolerance of 0.2 on coefficient of variation of area fraction as  $L_H = 96\ \mu\text{m}$  as shown in Fig. 6. The MDP process begins by dividing the computational domain  $\Omega_{comp}$  into six subdomains. This initial partition is shown in Fig. 7(a). Successive partitioning progresses according to the refinement criteria in Sec. 2.3, till the subdomain size reaches  $L_H$ . After three cycles of successive refinement, the partition size reaches  $L_H = 96\ \mu\text{m}$ . The final partitioned computational domain is shown in Fig. 7(b). The size of the inhomogeneous domain is  $\sim 48\ \mu\text{m}$ . The inhomogeneous regions identified by the MDP process should be modeled at the micromechanical level in the concurrent multiscale analyses. One of two such regions marked with dark box in Fig. 7(b) is shown in Fig. 8(a).

### 3. Locally Enriched VCFEM (LE-VCFEM) for Micromechanical Modeling of Ductile Fracture in Heterogeneous Microstructures

The Voronoi cell finite element model naturally evolves by tessellation of the microstructure into a network of multisided Voronoi cells. Each Voronoi cell

represents the neighborhood of particles or inclusions in the microstructure. The particles may be represented as ellipses or as multisided polygons. The particles are assumed to be brittle elastic materials while the matrix is assumed to be ductile and represented by a pressure dependent elasto-plastic model for porous material.

The VCFEM formulation is based on the assumed stress hybrid formulation,<sup>8–10</sup> in which equilibrated stress fields are assumed in the interior of each element and compatible displacements are assumed on the element boundary and on the particle–matrix interface. After particle cracking, the topology of each element changes from two constituent phases to three constituents with the inclusion of the crack, as shown in Fig. 9. In the subsequent ductile fracture phase, localized regions of softening in each Voronoi cell is enriched adaptively with finite deformation, displacement-based finite elements. The enriched Voronoi cell consists of the matrix phase  $\Omega_m$ , the particle phase  $\Omega_c$ , and a softening region of ductile damage  $\Omega_s$  is shown in Fig. 10.

Particle cracking in the microstructure naturally gives rise to stress concentrations or singularities, which in turn cause local matrix failure. With continued deformation beyond particle cracking, material points in the matrix lose their load

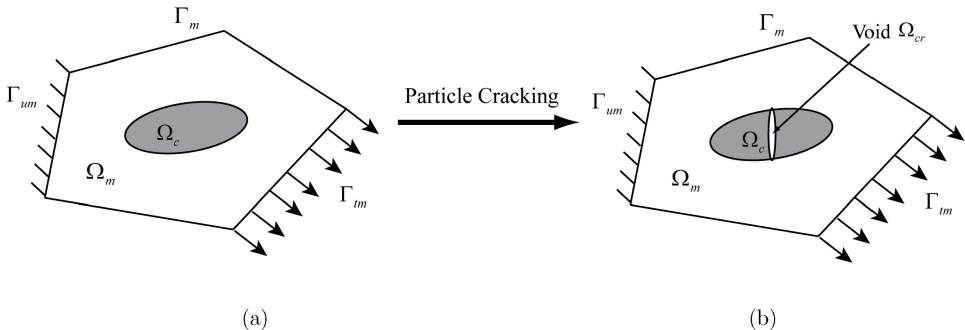


Fig. 9. Evolution of a Voronoi cell element (a) without damage and (b) with particle cracking.

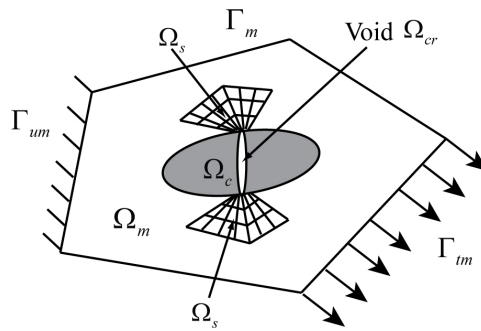


Fig. 10. Enriched VCFEM with superposed displacement elements in the softening region  $\Omega_s$ .

carrying capacity due to local void growth and strain softening. These regions are identified and adaptively converted to softened regions  $\Omega_s$ , for which a displacement-based finite element mesh is automatically generated. The region  $\Omega_s$  is modeled using finite deformation kinematics in which the rotated Cauchy stress rate<sup>28</sup> is used as an objective stress measure. Stresses  $\sigma_{ij}^s$  are evaluated using a backward Euler integration rule.<sup>29</sup> Mesh refinement using a  $h$ -type of refinement strategy is used to reduce error in the localization zone. A summary of the LE-VCFEM formulation is presented next.

### 3.1. VCFEM formulation with particle cracking

For particle cracking in an elastic–plastic matrix, an incremental element energy functional  $\Pi_e^{PC}$  is defined for each Voronoi cell element in terms of stress increments in the matrix and particle phases  $\Omega_m \cup \Omega_c$ , and displacement increments on the element boundary  $\partial\Omega_e$ , particle–matrix interface  $\partial\Omega_c$  as well as on the crack boundary  $\partial\Omega_{cr}$ . The first variation of  $\Pi_e^{PC}$  is expressed as:

$$\begin{aligned} \delta\Pi_e^{PC}(\Delta\sigma_{ij}, \Delta\bar{u}_i) = & - \int_{\Omega_m \cup \Omega_c} \Delta\varepsilon_{ij}\delta\Delta\sigma_{ij}d\Omega - \int_{\Omega_m \cup \Omega_c} \varepsilon_{ij}\delta\Delta\sigma_{ij}d\Omega \\ & + \int_{\partial\Omega_e} \delta\Delta\sigma_{ij}n_j^e\Delta\bar{u}_id\partial\Omega + \int_{\partial\Omega_e} (\sigma_{ij} + \Delta\sigma_{ij})n_j^e\delta\Delta\bar{u}_id\partial\Omega \\ & - \int_{\Gamma_{tm}} (\bar{\mathbf{t}}_i + \Delta\bar{\mathbf{t}}_i)\delta\Delta u_id\Gamma - \int_{\partial\Omega_c} (\delta\Delta\sigma_{ij}^m - \delta\Delta\sigma_{ij}^c)n_j^c\Delta\bar{u}'_id\partial\Omega \\ & - \int_{\partial\Omega_c} (\sigma_{ij}^m + \Delta\sigma_{ij}^m - \sigma_{ij}^c - \Delta\sigma_{ij}^c)n_j^c\delta\Delta\bar{u}'_id\partial\Omega \\ & - \int_{\partial\Omega_{cr}} \delta\Delta\sigma_{ij}^cn_j^{cr}\Delta\bar{u}''_id\partial\Omega - \int_{\partial\Omega_{cr}} (\sigma_{ij}^c + \Delta\sigma_{ij}^c)n_j^{cr}\delta\Delta\bar{u}''_id\partial\Omega. \end{aligned} \quad (9)$$

Here  $\bar{\mathbf{t}}$  is the external traction on the traction boundary  $\Gamma_{tm}$  and  $\mathbf{n}$  is the outward normal on respective boundary segments. The corresponding total energy functional for the entire computational domain is expressed as  $\sum_{e=1}^{NEL} \Pi_e^{PC}$ . The equilibrated stress field  $\Delta\sigma_{ij}$  is interpolated independently in the matrix and particle phases of the Voronoi cell. Conveniently, the Airy’s stress function  $\Phi(x, y)$  may be used to derive the equilibrated stress increments in the VCFEM formulation for rate-independent elasto-plasticity.<sup>8–10</sup> Compatible displacement fields  $\Delta\bar{u}_i$  are independently interpolated on the element/particle/crack boundaries using standard shape functions. Complete particle cracking is assumed to occur at the onset of damage, thereby avoiding crack propagation within each particle. A high aspect ratio ellipse ( $a/b = 10$ ) is used to represent the crack in the particle. The particle crack initiation criterion is expressed in the form of a Weibull probability function that depends on the local principal stresses and the volume fraction of the

particles in the microstructure.<sup>8,9</sup> For the  $i$ th particle, the fracture probability  $P_i$  is expressed as:

$$P_i(v, \sigma_i^I) = 1 - \exp\left[-\frac{v}{v_0} \left(\frac{\sigma_i^I}{\sigma_w}\right)^m\right], \quad (10)$$

where  $m$  and  $\sigma_w$  are the Weibull modulus and the characteristic strength, respectively.  $v$  is the volume of the  $i$ th particle.  $v_0$  is reference volume which is taken as the average volume of all particles and  $\sigma_i^I$  is the maximum principal stress in the  $i$ th particle.

### 3.2. Particle and matrix cracking causing ductile fracture

Ductile failure occurs by the combined phenomena of crack nucleation, microvoid growth and eventual void coalescence. Voids nucleate in the form of particle fragmentation, subsequently grow in the matrix with large plastic deformation, and finally coalesce with each other to advance the local fracture zone. A nonlocal form of the Gurson–Tvergaard–Needleman (GTN) model proposed in Refs. 17 and 18 is used to model the post-nucleation ductile fracture in the matrix material. In this model, a pressure-dependent yield surface  $\Phi$  is written in terms of the evolving void volume fraction  $f^*$  as:

$$\Phi = \left(\frac{q}{\sigma_0}\right)^2 + 2f^*q_1 \cosh\left(-\frac{3q_2 p}{2\sigma_0}\right) - (1 + q_3 f^{*2}), \quad (11)$$

where  $q$  and  $p$  are respectively the Von-Mises stress and hydrostatic pressure in the matrix, and  $q_1, q_2, q_3$  are constants calibrated from numerical analyses of a periodic array of voids.  $\sigma_0(\varepsilon^p)$  is the strength of the matrix material in the absence of voids. To avoid mesh sensitivity of numerical failure predictions, a nonlocal evolution equation for the void volume fraction is implemented. The nonlocal void volume fraction growth rate at a material point  $\mathbf{x}$  is written as:

$$\begin{aligned} \dot{f}_{nl} &= \frac{1}{W(\mathbf{x})} \int_{\Omega_m} \dot{f}(\bar{\mathbf{x}}) w(|\mathbf{x} - \bar{\mathbf{x}}|) d\Omega; \quad W(\mathbf{x}) = \int_{\Omega_m} w(|\mathbf{x} - \bar{\mathbf{x}}|) d\Omega, \\ w(z) &= \left[ \frac{1}{1 + (z/L)^p} \right]^q, \quad p = 8, \quad q = 2. \end{aligned} \quad (12)$$

The weighting function  $w(z)$  has a value close to 1 within a region of characteristic length scale radius  $L$  ( $z \leq L$ ) and diminishes rapidly outside this region. The local void growth rate is governed by the relation:

$$\dot{f} = (1 - f_{nl}) \dot{\epsilon}_{kk}^p + A(\bar{\varepsilon}^p) \dot{\bar{\varepsilon}}^p, \quad (13)$$

where the evolution of effective plastic strain is written as:

$$\sigma_0 \dot{\bar{\varepsilon}}^p = \sigma_{ij} \dot{\lambda} \frac{\partial \Phi}{\partial \sigma_{ij}}. \quad (14)$$

The second term in Eq. (13) is for strain-controlled void nucleation,<sup>30</sup> where

$$A = \frac{f_N}{s_N \sqrt{2\pi}} \exp \left[ -\frac{1}{2} \left( \frac{\bar{\varepsilon}^p - \varepsilon_N}{s_N} \right)^2 \right]. \quad (15)$$

For void coalescence, an acceleration function proposed in Ref. 31 is used,

$$f^* = \begin{cases} f_{nl} & f_{nl} \leq f_c, \\ f_c + \frac{f_u^* - f_c}{f_f - f_c} (f_{nl} - f_c) & f_{nl} > f_c. \end{cases} \quad (16)$$

Here  $f_c$  is the critical void volume fraction at which void coalescence first occurs and  $f_f$  is the value at final failure. The material loses all load capacity as  $f_{nl} \rightarrow f_f$ , i.e.,  $f^* \rightarrow f_u^* = 1/q_1$ .

A problem with the stress-based VCFEM is that nonuniqueness in the displacement solutions in the softening phase of stress-strain relation results in numerical instabilities. To avert this shortcoming, the softening region  $\Omega_s$  within each Voronoi cell element is adaptively augmented with displacement-based finite elements as shown in Fig. 10. Finite deformation, pressure-dependent elasto-plasticity formulation is used for the displacement-based elements in  $\Omega_s$ .

Superscript  $s$  corresponds to variables associated with  $\Omega^s$ . The LE-VCFEM formulation guarantees that displacement  $\mathbf{u}^s$  on the boundary  $\partial\Omega_s$  are compatible with the displacement  $\bar{\mathbf{u}}$ ,  $\bar{\mathbf{u}}'$ , and  $\bar{\mathbf{u}}''$  respectively on the  $\partial\Omega_m$ ,  $\partial\Omega_c$ , and  $\partial\Omega_{cr}$ , i.e.,

$$\begin{aligned} \mathbf{u}^s = \bar{\mathbf{u}} & \text{ on } \partial\Omega_s \cap \partial\Omega_m; & \mathbf{u}^s = \bar{\mathbf{u}}' & \text{ on } \partial\Omega_s \cap \partial\Omega_c; \\ \mathbf{u}^s = \bar{\mathbf{u}}'' & \text{ on } \partial\Omega_s \cap \partial\Omega_{cr}. \end{aligned} \quad (17)$$

With the addition of  $\Omega_s$ , the VCFEM formulation is modified with an augmentation of the energy functional of Eq. (9). The corresponding incremental potential energy for the displacement elements is added to the incremental element energy functional  $\Pi_e^{PC}$  to yield an enriched energy functional  $\Pi_e^{EN}$  with an added independent variable  $\Delta\mathbf{u}^s$ . The corresponding first variation of  $\Pi_e^{EN}$  is:

$$\begin{aligned} \delta\Pi_e^{EN}(\Delta\sigma_{ij}, \Delta\bar{u}_i, \Delta u_i^s) = \delta\Pi_e^{PC} - & \int_{\Omega_s} (\sigma_{ij}^s + \Delta\sigma_{ij}^s) \delta\Delta\varepsilon_{ij}^s d\Omega \\ & + \int_{\partial\Omega_s} \delta\Delta\sigma_{ij} n_j^s \Delta u_i^s d\partial\Omega + \int_{\partial\Omega_s} (\sigma_{ij} + \Delta\sigma_{ij}) n_j^s \delta\Delta u_i^s d\partial\Omega, \end{aligned} \quad (18)$$

where  $\Delta u_i^s$  is the displacement increment. The displacement interpolation in terms of the nodal displacements are expressed as:

$$\{\Delta\mathbf{u}^s\} = \{\mathbf{N}^s\}\{\Delta\mathbf{q}^s\}. \quad (19)$$

The adapted LE-VCFEM couples small deformation hybrid stress-based region  $\Omega_m$  and a finite deformation displacement-based softening region  $\Omega_s$ . This necessitates different integration algorithms for elements in different regions. In the

hybrid stress-based region, a strain update algorithm implementing the *Regula Falsi* scheme is used to calculate plastic strains, stresses, and state variables for given stress increments  $\Delta\sigma$ .<sup>8,9</sup> For the displacement elements, a backward Euler method proposed in Ref. 29 is used for stress and plastic strain update in an updated Lagrangian formulation introduced in Ref. 28. The constitutive equations are written in terms of the objective rate of the rotated Cauchy stress  $\sigma_R^s = \mathbf{R}^T \sigma^s \mathbf{R}$ , in which  $\mathbf{R}$  is a proper orthogonal tensor obtained from the polar decomposition of  $\mathbf{F}$ . The rotated Cauchy stress is updated to the  $(n+1)$ th increment using the equation

$$(\sigma_R^s)^{n+1} = (\sigma_R^s)^n + \Delta\sigma_R^s; \quad \Delta\sigma_R^s = (\mathbf{C}^{e-p})^{n+1} : \Delta\varepsilon_R^s, \quad (20)$$

where  $\mathbf{C}^{e-p}$  is the elasto-plastic tangent stiffness in the rotated configuration:

$$C_{ijkl}^{e-p} = \left( \frac{\partial(\sigma_R^s)_{ij}}{\partial(\varepsilon_R^s)_{kl}} \right). \quad (21)$$

An iterative solution procedure is used in the backward Euler integration method.

Once displacement elements are identified and superposed in the softening regions in LE-VCFEM, it is important to map all the parameters, e.g., stress, strain, and other internal variables from the assumed stress model with stress interpolations to the assumed displacement elements. The super-convergent patch recovery or SPR method developed in Ref. 32 is used to map values from the VCFE mesh to nine-noded Lagrange polynomial displacement elements. In this process, a complete 4th order polynomial expansion is used for all parameters.

### 3.3. A numerical example of ductile failure in reinforced aluminum microstructure

Figure 9(a) shows the micrograph of aluminum alloy consisting of silicon particles. Figure 9(c) shows the corresponding Voronoi cell mesh for an equivalent simulated microstructure. The Al matrix is assumed to be ductile and is modeled by elastic–plasticity constitutive relations for porous materials with the following properties: Young's modulus  $E = 66$  GPa, Poisson's ratio  $v = 0.33$ , initial void volume fraction  $f_0 = 0.004$ . The post yield behavior for the pure matrix material without voids is expressed by the Ramberg–Osgood law ( $\sigma_m = \sigma_0(\varepsilon_m^p/\alpha\varepsilon_0)^{1/n}$ ), where the initial flow stress in the matrix  $\sigma_0 = 440$  MPa,  $\varepsilon_0$  is the strain at yield ( $\varepsilon_0 = \sigma_0/E$ ),  $\alpha = 3/7$  and the strain hardening exponent  $n = 12.5$ . The silicon particles are assumed to be brittle and are modeled with the linear elastic properties: Young's modulus  $E = 400$  GPa, Poisson's ratio  $v = 0.2$ . For particle cracking, ( $m = 2.4$ ,  $\sigma_w = 1.32$  GPa) are used in Eq. (10) for Weibull model. For the GTN model, ( $q_1 = 1.5$ ,  $q_2 = 1.0$ ,  $q_3 = q_1^2 = 2.25$ ) are used in Eq. (11) and  $L = 0.05 \times$  (maximum size of the Voronoi cell elements) is used in Eq. (12) for the nonlocal model. The parameters ( $\varepsilon_N = 0.1$ ,  $s_N = 0.1$ ,  $f_N = 0.1$ ) are used in Eq. (15) for nucleation. The microstructure is subjected to a macroscopic tension strain  $\bar{\varepsilon}_{xx} = 1.57\%$ , applied on the left side of the model. The results of the simulation are shown in Fig. 11.

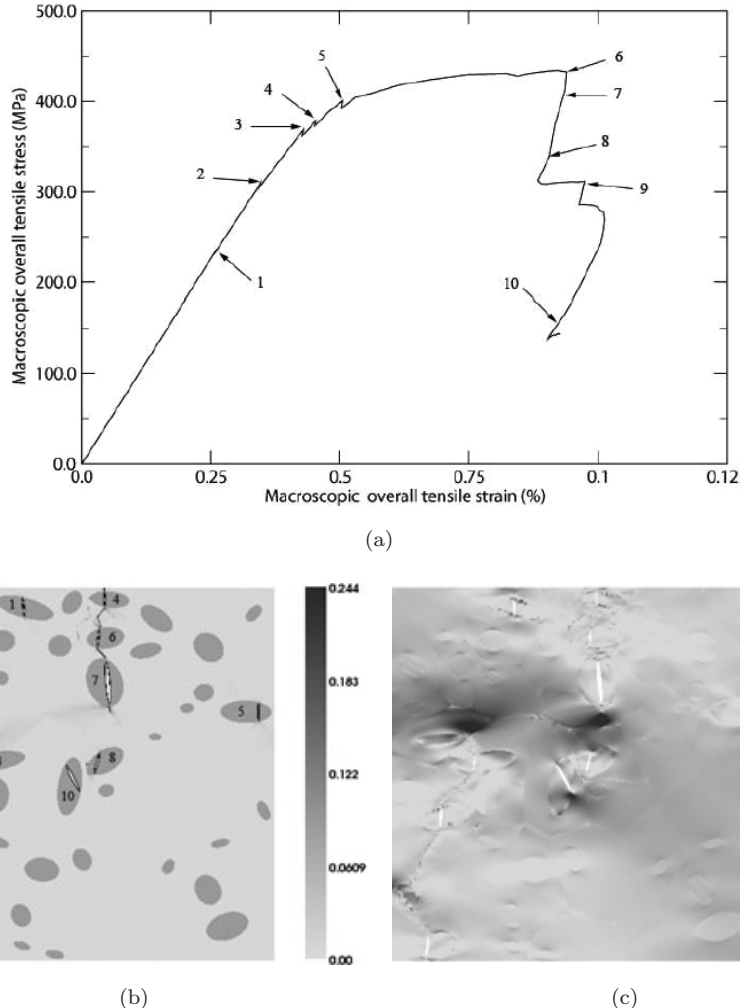


Fig. 11. (a) Macroscopic strain–stress response; contour plot of (b) the void volume fraction and (c) the stress  $\sigma_{xx}$  (GPa) at  $\bar{\varepsilon}_{xx} = 1.57\%$ . The numbers in (a) and (b) indicate the sequence of particle cracking.

Figure 11(a) shows the macroscopic strain–stress response, with the explicit effect of particle cracking followed by ductile matrix fracture. The cracked particle numbers are shown in Fig. 11(b). The first nine particles crack in isolation and do not show any softening in the stress–strain behavior. Softening, manifested by a drop in the stress–strain curve, starts after the tenth particle has cracked followed by significant plastic deformation and void growth in the matrix. From Fig. 11(b), it is evident that the subsequent sequence of particle and matrix cracking occur in a very narrow band of the microstructure and hence a dominant crack path is observed. The sequence of particle cracking is shown in the stress–strain plot of Fig. 11(a).

The figure shows that particles 6, 7, 8, 9, and 10 crack after the dominant ductile crack has developed in the microstructure. Contour plots of the void volume fraction and the stress in the loading direction for  $\bar{\varepsilon}_{xx} = 1.57\%$  are shown in Figs. 11(b) and 11(c). Near the dominant fracture path, the stress  $\sigma_{xx}$  decreases to near zero.

#### 4. Homogenization-Based Continuum Damage Mechanics Model for Plasticity with Void Evolution

In this section, a homogenization-based anisotropic plasticity-damage (HAPD) model is developed for ductile materials containing nonuniform dispersion of brittle particles. Underlying damage mechanisms are particle cracking and void growth and coalescence in the microstructure. The HAPD model is chosen to follow the general framework of the Gurson–Tvergaard–Needleman model.<sup>30,31</sup> To accommodate nonproportional loading, the HAPD models are expressed in the principal material coordinate system. The model is developed for plane strain problems in this paper. The anisotropic yield criterion for porous ductile materials containing a dispersion of particles depend on hydrostatic stress measures and void volume fraction is written as:

$$\phi = \frac{\Sigma_{eq}^2}{Y_f^2(W_p)} + 2Q_1 f \cosh\left(\frac{Q_a \Sigma_{xx} + Q_b \Sigma_{yy} + Q_c \Sigma_{zz}}{Y_f(W_p)}\right) - 1 - (Q_1 f)^2 = 0, \quad (22)$$

where  $\Sigma_{ij}$  is the homogenized stress in the composite medium,  $W_p$  is plastic work,  $f$  is void volume fraction and  $Y_f$  is the matrix flow stress in shear. The increment of macroscopic plastic strain is obtained from the yield criterion by using an associated flow rule for hardening materials, i.e.,  $\dot{\epsilon}_{ij}^p = \dot{\lambda} \partial\phi/\partial\Sigma_{ij}$ . This yield criterion is defined in the principal axes of material anisotropy to accommodate nonproportional loading. Material anisotropy is determined not only by the morphology of microstructures, such as size, shape and distribution of particles, but also the evolution of plastic deformation and damage in the microstructure during loading process. The material is assumed to be orthotropic with respect to the principal coordinate system. It is assumed that at every load step, material remains orthotropic with respect to the evolving material axis. At every step, the angle  $\beta$  in Fig. 12 corresponding to principal axes of anisotropy for plane strain is determined from the conditions required to keep the tangent modulus  $E_{ijkl}^{\tan}$  orthotropic. Consequently, terms coupling the normal and shear components in the transformed tangent modulus are set to zero, i.e.,  $(E_{1112}^{\tan})' = (E_{2212}^{\tan})' = (E_{3312}^{\tan})' = 0$ , where

$$(E_{ijkl}^{\tan})' = Q_{im} Q_{jn} Q_{kp} Q_{lq} E_{mnpq}^{\tan} \quad \text{and} \quad [\mathbf{Q}] = \begin{bmatrix} \cos\beta & \sin\beta & 0 \\ -\sin\beta & \cos\beta & 0 \\ 0 & 0 & 1 \end{bmatrix}. \quad (23)$$

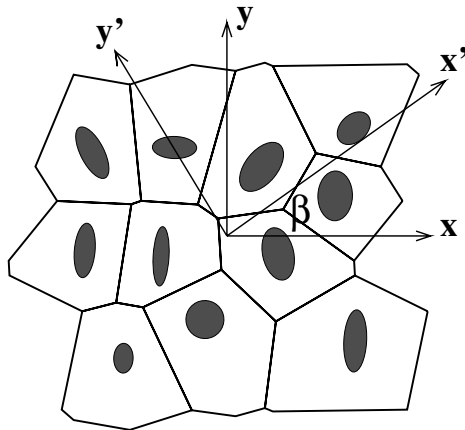


Fig. 12. RVE's showing principal axes of material anisotropy.

Parameters in the HAPD model are calibrated by comparing macroscopic analysis data with those obtained from homogenizing results of micromechanical RVE analysis. The asymptotic expansion-based homogenization of microscopic variables in the microstructural RVEs using periodicity assumptions on the boundary has been discussed in Refs. 11 and 12. The micromechanical analysis is done using LE-VCFEM discussed in Sec. 3. For plane strain, the equivalent stress in the equivalent material without voids (matrix and particles only) is represented using Hill's<sup>33</sup> anisotropic yield function as:

$$\Sigma_{eq}^2 = F(\Sigma_{yy} - \Sigma_{zz})^2 + G(\Sigma_{zz} - \Sigma_{xx})^2 + H(\Sigma_{xx} - \Sigma_{yy})^2 + C\Sigma_{xy}^2. \quad (24)$$

The matrix anisotropy parameters  $F, G, H, C$  are calibrated from homogenization studies with material without voids. Likewise, parameters  $Q_1, Q_a, Q_b$ , and  $Q_c$  corresponding to an effective hydrostatic stress are calibrated from homogenization studies on materials containing voids. Most anisotropic plastic models in the literature, e.g., Refs. 21 and 34, assume constant anisotropy parameters that do not evolve with deformation. However, anisotropy parameters calibrated in Sec. 4.1, for different RVEs shows significant evolution with deformation. To test if the constant parameters in the HAPD model can produce good agreement with homogenized micromechanics analysis, tension tests are conducted for an RVE with a circular particle of 20% volume fraction in a square matrix. Homogenized results of micromechanical analyses are compared with macroscopic analysis using the yield criterion (24). First, isotropic parameters:  $F = G = H = Q_a = Q_b = Q_c = 0.5$ ,  $Q_1 = 1.5$ , and  $C = 3.0$  are used in the macroscopic analysis. Second, only initial anisotropy parameters:  $F = 0.56$ ,  $G = 0.56$ ,  $H = 0.45$ ,  $C = 3.0$ ,  $Q_1 = 1.5$ ,  $Q_a = 0.46$ ,  $Q_b = 0.46$ , and  $Q_c = 0.55$ , calibrated in the following section are used for the macroscopic analysis. The equivalent stress is compared for macroscopic

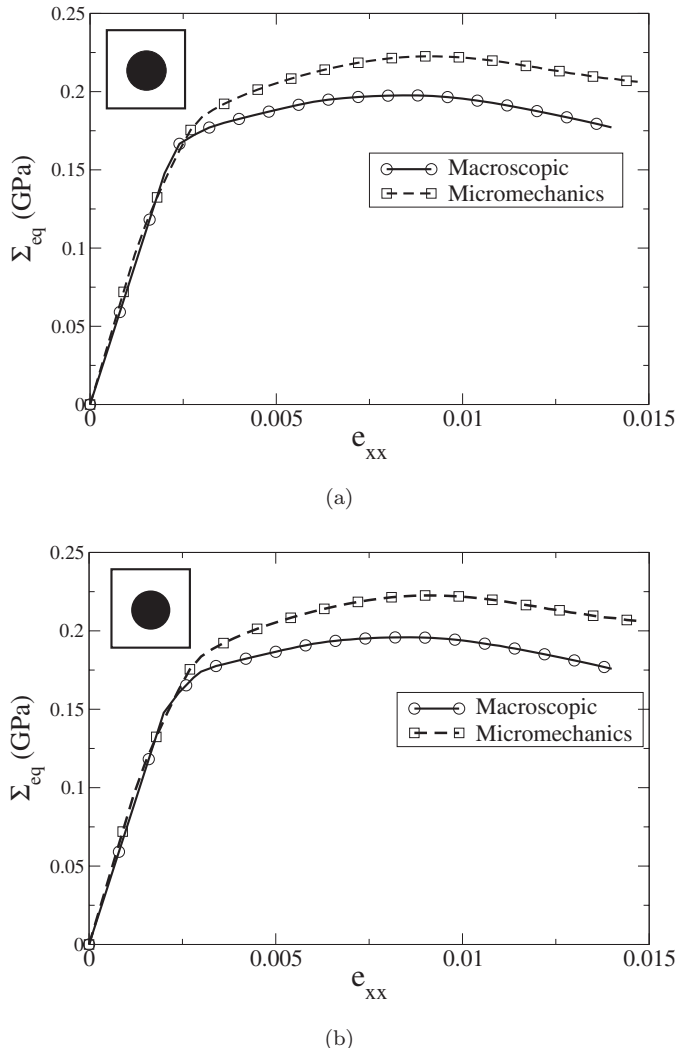


Fig. 13. Comparison of equivalent stress by macroscopic model with isotropic parameters with that by micromechanics RVE analysis (a) macroscopic analysis with isotropic parameters and (b) macroscopic analysis with initial anisotropic parameters.

analysis with the HAPD model and micromechanics RVE analysis in Fig. 13. Figure 13(a) shows that because of the existence of second-phase particle, isotropic parameters are not suitable for macroscopic analysis even for a simple RVE. Figure 13(b) clearly demonstrates that constant anisotropy parameters are not able to produce good match with micromechanics analysis results, and evolution of anisotropy parameters must be considered in the calibration process. The anisotropy parameters are found to be functions of the plastic work ( $W_p$ ) in this work.

#### 4.1. Evaluation of constitutive parameters in the homogenized constitutive model

##### 4.1.1. $Y_f(W_p)$ and $C$

As defined in Eq. (22),  $Y_f(W_p)$  is taken as the flow stress in shear. A microscopic boundary value problem of the RVE is solved for pure shear loading:  $e_{xx} = e_{yy} = 0$ ,  $e_{xy} \neq 0$ , which is followed by homogenization. A macroscopic shear strain is applied on the RVE with periodic boundary conditions, detailed in Ref. 12. The macroscopic plastic work, stress, and strains are evaluated by averaging microstructural variables using the relations:

$$\dot{W}_p = \frac{1}{\Omega} \int_{\Omega} \sigma_{ij} \dot{\varepsilon}_{ij}^p d\Omega, \quad \Sigma_{ij} = \frac{1}{\Omega} \int_{\Omega} \sigma_{ij} d\Omega, \quad e_{ij} = \frac{1}{\Omega} \int_{\Omega} \varepsilon_{ij} d\Omega. \quad (25)$$

For pure shear loading condition,  $\Sigma_{xx} = \Sigma_{yy} = \Sigma_{zz} = 0$  and  $\Sigma_{xy} \neq 0$ . The parameter  $C$  in Eq. (24) is first set to 3, such that  $Y_f(W_p) = \sqrt{3}\Sigma_{xy}$ . Finally, the flow stress is plotted as a function of  $W_p$  as shown in Fig. 14(a).

##### 4.1.2. Parameters $F$ , $G$ , and $H$

- (i) A set of numerical experiments for the RVE (without voids or particle fragmentation) for different loading conditions are performed using LE-VCFEM and homogenization theory. The different loading conditions are represented by various macroscopic strain combinations  $e_{xx}:e_{yy}:e_{xy} = a:b:c$ . A total of 13 numerical experiments are performed; the corresponding strain combinations are: 1:0:0; 0:1:0; 2:1:0; 1:2:0; 1:1:0; 1:0:2; 0:1:2; 1:0:4; 0:1:4; 2:1:2; 1:2:2; 1:1:2 and 1:1:4. Macroscopic stress and plastic work are obtained for each case in the principal axes of anisotropic from Eq. (25). For each loading condition, macroscopic stresses in principal axes of anisotropy are plotted as functions of plastic work  $W_p$ , as shown in Fig. 14(b).
- (ii) For a given value of macroscopic plastic work, the yield stress  $Y_f(W_p)$  is obtained from the plot discussed in Sec. 4.1.1. Macroscopic stress components are obtained as functions of  $W_p$  for different loading conditions from the plots in step (i), as shown in Fig. 14(b). Anisotropy parameters  $F$ ,  $G$ , and  $H$  in Eq. (24) are obtained by minimizing the function  $\sum_{i=1}^{13} \phi_i^2(F, G, H)$  using the least square method for macroscopic plastic work corresponding to 13 numerical experiments. This step is repeated for different values of  $W_p$  and the anisotropy parameters are plotted as functions of  $W_p$ .

##### 4.1.3. Parameters $Q_1$ , $Q_a$ , $Q_b$ , and $Q_c$

- (i) A macro-micro pure shear problem is solved with RVE homogenization for matrix material containing a nonzero initial void volume fraction. The macroscopic stresses and averaged void volume fraction are plotted as functions

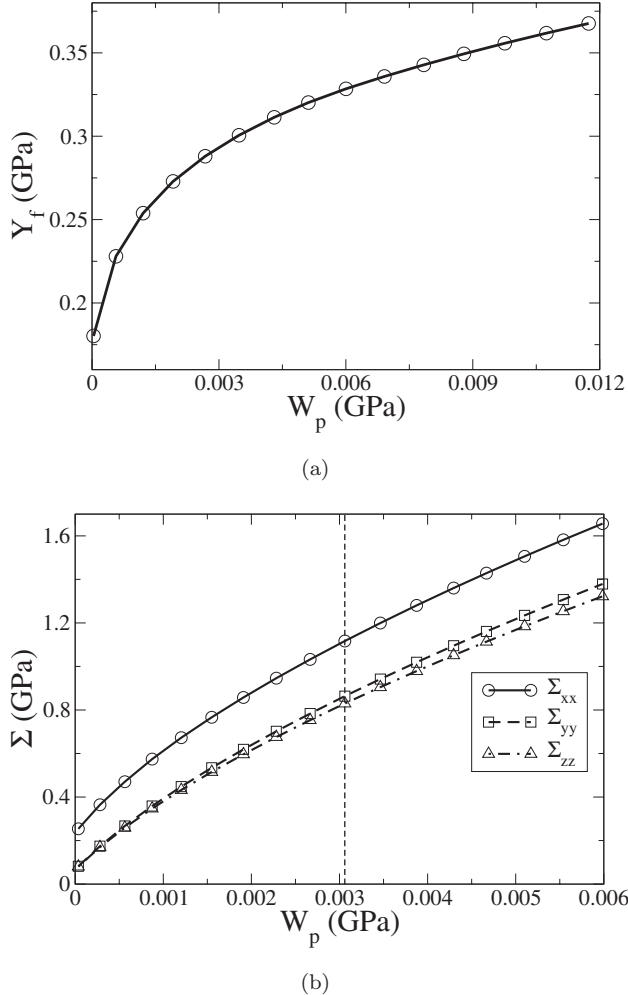


Fig. 14. (a) Yield stress as a function of macroscopic plastic work and (b) macroscopic stresses as functions of macroscopic plastic work.

of  $W_p$ , where the averaged rate of plastic work is

$$\dot{W}_p = \frac{1}{\Omega} \int_{\Omega} \frac{1}{1-f} \sigma_{ij} \dot{\varepsilon}_{ij}^p d\Omega .$$

$Q_1$  can be determined directly by solving the following yield equation with different  $\Sigma_{xy}$  and corresponding  $Y_f$ :

$$\frac{3\Sigma_{xy}^2}{Y_f^2} + 2Q_1f - (1 + Q_1^2f^2) = 0 . \quad (26)$$

- (ii) The same set of numerical experiments used in Sec. 4.1.2 is performed again for the matrix material containing a nonzero initial void volume fraction.

- (iii) Again, considering that the plastic work is invariant with respect to the loading condition, parameters  $Q_a$ ,  $Q_b$ ,  $Q_c$  are evaluated by minimizing  $\sum_{i=1}^{13} \phi_i^2(Q_a, Q_b, Q_c)$  using the least square method. This step is repeated for different values of  $W_p$ , and  $Q_a$ ,  $Q_b$ , and  $Q_c$  are plotted as functions of  $W_p$ .

#### 4.1.4. Void nucleation equations

Particle cracking in the microstructure is a source of void nucleation in the macroscopic HAPD model. Figure 15 shows the averaged stress-strain behavior for a microstructure containing 20 particles that incurs particle cracking. Every time a particle cracks, there is a drop in the stress-strain curve resulting in discontinuities. However, the homogenized stress-strain behavior with the HAPD model will exhibit a continuous behavior due to the introduction of continuous functions in the void nucleation model.

The void nucleation model is based on a modified form of the second term of Eq. (13), in which the coefficient  $A(\bar{e}^p)$  is developed from results of micromechanical simulations of an RVE. The fraction of cracked particles in microstructure, observed in the RVE simulations, may be modeled using a two-parameter Weibull distribution function  $F(\bar{e})$ , expressed as<sup>8,9,16</sup>:

$$F(\bar{e}^p) = 1 - \exp\left[-\left(\frac{\bar{e}^p}{e_o}\right)^m\right], \quad (27)$$

where  $e_o$ ,  $m$  are Weibull parameters to be calibrated, and  $\bar{e}^p = I_1 + I_2$  is a function of strain invariants  $I_1$ ,  $I_2$ , defined as:

$$\begin{aligned} I_1 &= Ae_{11}^p + Be_{22}^p + Ce_{33}^p, \\ I_2 &= D(e_{22}^p - e_{33}^p)^2 + E(e_{33}^p - e_{11}^p)^2 + F(e_{11}^p - e_{22}^p)^2. \end{aligned} \quad (28)$$

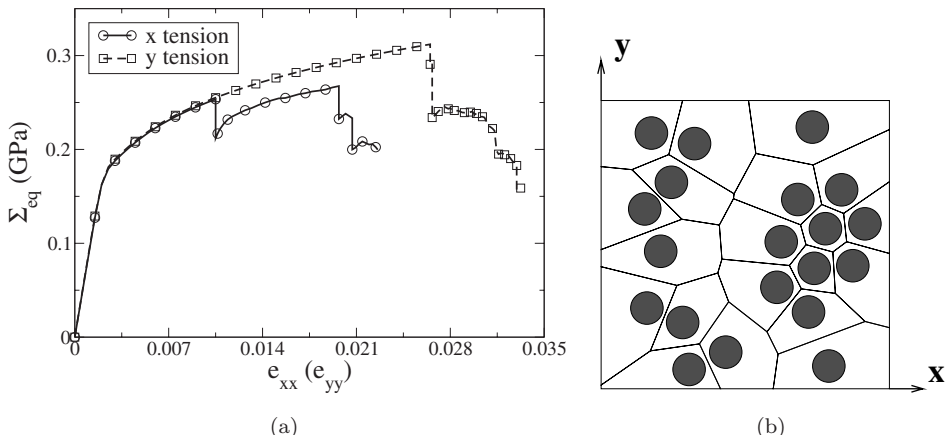


Fig. 15. (a) Equivalent stress–strain curves and (b) microstructure.

Here  $e_{11}^p$ ,  $e_{22}^p$ ,  $e_{33}^p$  are the principal components of plastic strains, and  $A$ ,  $B$ ,  $C$ ,  $D$ ,  $E$ ,  $F$  are parameters that can be calibrated from micromechanically determined values of nucleation strains for different loadings. The nucleation coefficient for macroscopic model may be written as:

$$A(\bar{e}^p) = v \frac{dF(\bar{e}^p)}{d\bar{e}^p}, \quad (29)$$

where  $v$  is a parameter that relates the microscopic volume fraction of cracked particles to the evolution of homogenized porosity due to void nucleation in the HAPD model.

Micromechanical simulations with five different loading conditions are conducted for calibration of parameters in Eq. (28). These include two tension tests (tension loading in a direction while constraining the other direction), two simple tension tests (tension loading in a direction keeping the other direction constraint free) and one bi-axial tension test. The tension test in the  $x$  direction is used as a reference loading conditions. The fraction of cracked particles for tension test on  $x$  direction is plotted as a function of strain  $e_{11}$  is shown in Fig. 16.

In Fig. 16, parameters  $e_o$ ,  $m$  are calibrated to fit the test data. The least square method is used with this reference curve to calibrate parameters  $A$ ,  $B$ ,  $C$ ,  $D$ ,  $E$ , and  $F$ . Finally,  $v$  is determined iteratively by matching results from micromechanics and macroscopic analysis.

#### 4.2. Numerical implementation of the HAPD model

In an incremental form of the constitutive model, the macroscopic stress increments  $\Delta\Sigma_{ij}$  are related to elastic increments of strains as:

$$\Delta\Sigma_{ij} = E_{ijkl}(\Delta e_{kl} - \Delta e_{kl}^p), \quad (30)$$

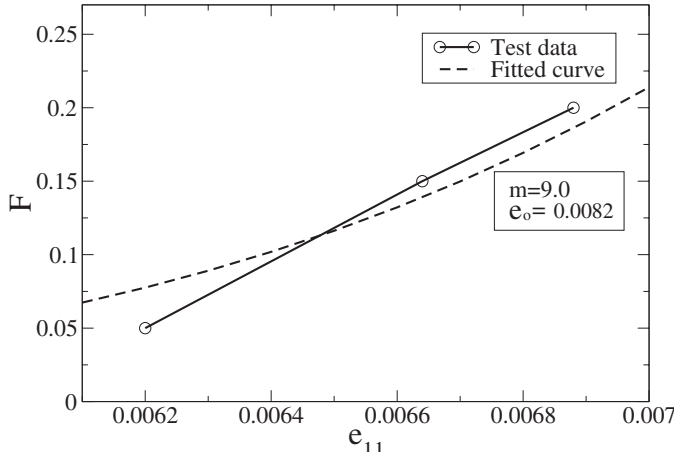


Fig. 16. Calibration of Weibull parameters.

where  $E_{ijkl}$  is the homogenized elastic tensor. Using associated flow rule, components of plastic strain increment are obtained as:

$$\begin{aligned}\Delta e_{xx}^p &= \Delta\lambda \frac{\partial\phi}{\partial\Sigma_{xx}}, & \Delta e_{yy}^p &= \Delta\lambda \frac{\partial\phi}{\partial\Sigma_{yy}}, \\ \Delta e_{xy}^p &= \Delta\lambda \frac{\partial\phi}{\partial\Sigma_{xy}}, & \Delta e_{zz}^p &= \Delta\lambda \frac{\partial\phi}{\partial\Sigma_{zz}}.\end{aligned}\quad (31)$$

Eliminating the flow parameter  $\Delta\lambda$  from Eq. (31) results in the set of equations

$$\begin{aligned}\Delta e_{xx}^p \left( \frac{\partial\phi}{\partial\Sigma_{yy}} \right) - \Delta e_{yy}^p \left( \frac{\partial\phi}{\partial\Sigma_{xx}} \right) &= 0, \\ \Delta e_{xx}^p \left( \frac{\partial\phi}{\partial\Sigma_{xy}} \right) - \Delta e_{xy}^p \left( \frac{\partial\phi}{\partial\Sigma_{xx}} \right) &= 0, \\ \Delta e_{xx}^p \left( \frac{\partial\phi}{\partial\Sigma_{zz}} \right) - \Delta e_{zz}^p \left( \frac{\partial\phi}{\partial\Sigma_{xx}} \right) &= 0.\end{aligned}\quad (32)$$

With known increments of strain, the set of Eq. (32), together with the yield function Eq. (22) are solved iteratively by using the Newton–Raphson method to obtain stress increments.

### 4.3. Numerical examples

The GTN model-based HAPD model is validated by comparing the results of a range of macroscopic numerical simulations with those obtained by coupled macro–microscale analysis using enriched LE-VCFEM and asymptotic homogenization for various RVEs. In this section, simulations are conducted for two heterogeneous microstructures, without and with voids. The RVEs considered are: (1) a square matrix domain with one circular and (b) an arbitrary shaped domain with 40 randomly distributed particles of different sizes and shapes. The RVE material properties for the matrix are  $E = 72$  GPa,  $v = 0.25$ . The post yield behavior for the pure matrix material without voids is expressed by the Ramberg–Osgood law ( $\sigma_m = \sigma_0(\varepsilon_m^p/\alpha\varepsilon_0)^{1/n}$ ), where the initial flow stress of the matrix is  $\sigma_0 = 440$  MPa,  $\varepsilon_0$  is the strain at yield ( $\varepsilon_0 = \sigma_0/E$ ), material parameter  $\alpha = 3/7$  and strain hardening exponent  $n = 12.5$ . For the brittle particles,  $E = 320$  GPa and  $v = 0.22$ .

#### 4.3.1. Simulations for microstructure without voids

Anisotropy parameters for the two RVEs are plotted in Figs. 17(a) and 18(a) as functions of  $W_p$ . The results of a pure macroscopic analysis using the anisotropic plasticity model are compared with pure micromechanic-based results that are averaged after each load step. The results of this comparison for the loading condition  $e_{xx}:e_{yy}:e_{xy} = 2:1:4$  are shown in Figs. 17(b) and 18(b) with good agreement. Comparisons for other loading conditions represented by various strain combinations (not shown) also show good agreement.

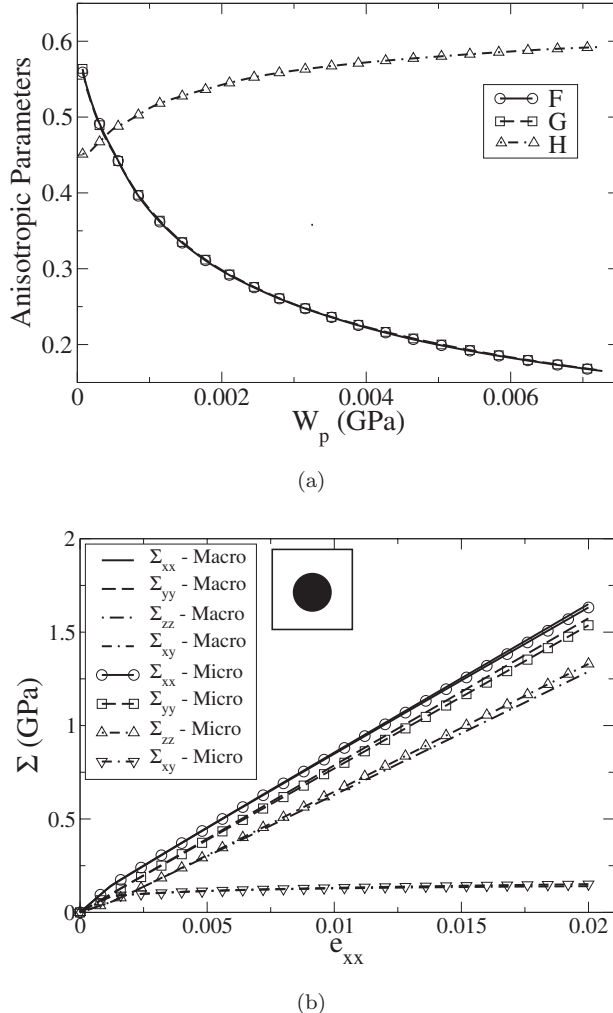


Fig. 17. (a) Anisotropic plastic yield parameters and (b) comparison of strain–stress response by the macroscopic constitutive model with that by microscopic RVE analysis with homogenization for a simple unit cell with one particle.

#### 4.3.2. Simulations for microstructure with voids

The same simulations of Sec. 4.3.1 are revisited for the two RVEs, now with 0.1% initial void volume fraction. The calibrated parameter  $Q_1$  shows that it does not change with plastic work for both RVEs,  $Q_1 = 1.5$ . The evolutions of parameters  $Q_a$ ,  $Q_b$ , and  $Q_c$  with  $W_p$  are shown in Figs. 19(a) and 20(a). The results of simulations by the anisotropic ductile damage model are compared with those by micromechanical RVE analysis with homogenization under the loading condition ( $e_{xx}:e_{yy}:e_{xy} = 2:1:4$ ) in Figs. 19(b) and 20(b). The results show good agreement.

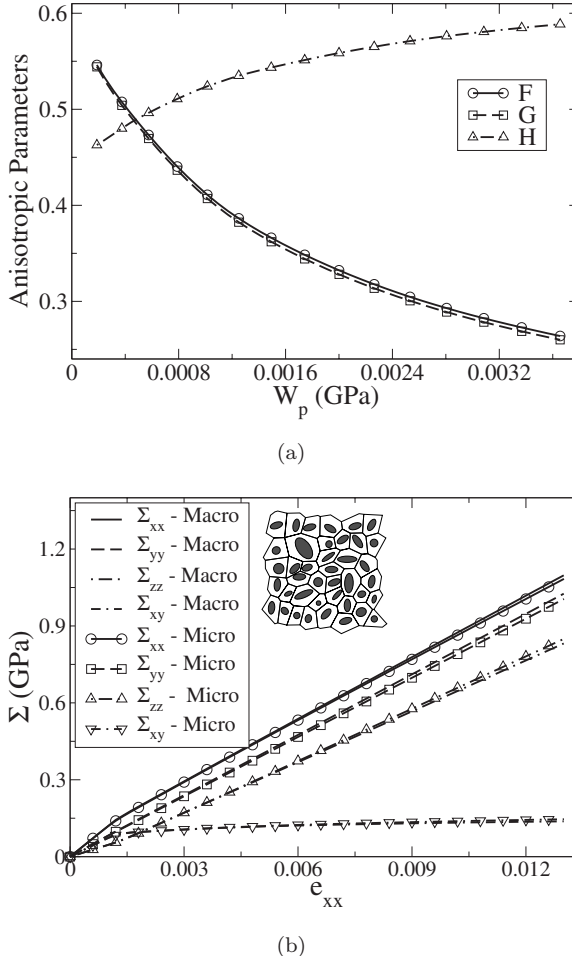


Fig. 18. (a) Anisotropic plastic yield parameters and (b) comparison of strain–stress response by the macroscopic constitutive model with that by microscopic RVE analysis with homogenization for an arbitrary RVE with 40 random distributed particles.

#### 4.3.3. Simulations for microstructure with particle and matrix cracking

For microstructure, shown in Fig. 15(b), several tests are conducted using both the macroscopic and micromechanics models. Parameters related to void nucleation in the macroscopic model are listed in Table 1. Equivalent stresses by macroscopic analyses are compared with that of micromechanics analyses in Fig. 21. The results of the HAPD model-based macroscopic analysis follow the softening trend closely and gives very good prediction of loss of loading capacity due to particle cracking. It also shows the difference of nucleation in different directions. These results indicate that the morphology plays a significant role in microstructural damage. Because of the existence of cluster on the right side of microstructure, it starts to

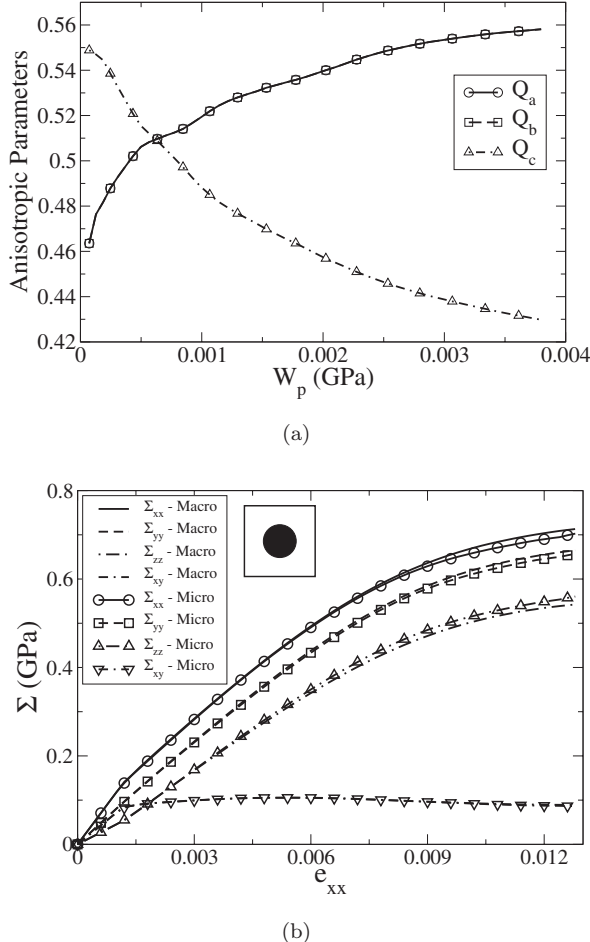


Fig. 19. (a) Anisotropic parameters for the hydrostatic portion of plastic yield and (b) comparison of strain–stress response by the macroscopic constitutive model with that by microscopic RVE analysis with homogenization for a simple unit cell with one particle.

lose its loading capacity for loadings in the  $x$  direction much earlier than in the  $y$  direction.

## 5. Conclusions

This paper develops three modules contributing to the overall framework of multiscale modeling of ductile fracture of metallic materials with nonuniformly dispersed particles, e.g., cast aluminum alloys. The first module introduces a morphology-based domain partitioning (MDP) algorithm as a preprocessor to multiscale modeling. MDP is instrumental in identifying regions of strong inhomogeneity in the

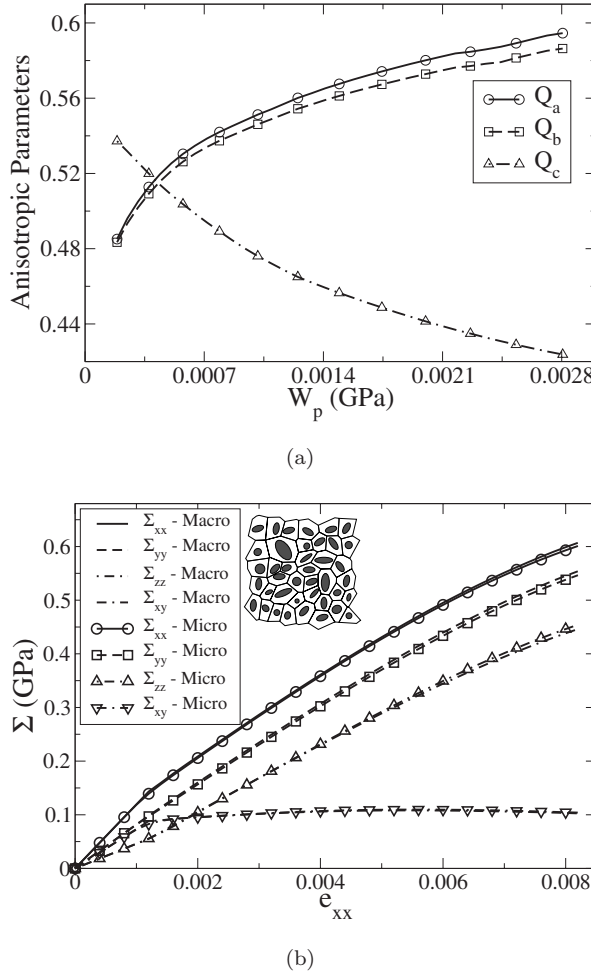


Fig. 20. (a) Anisotropy parameters for the hydrostatic portion of plastic yield and (b) comparison of strain-stress response by the macroscopic constitutive model with that by microscopic RVE analysis with homogenization for an arbitrary RVE with 40 random distributed particles.

Table 1. Void nucleation parameters.

$A$	$B$	$C$	$D$	$E$	$F$	$v$
1.14	1.06	—	-147.97	-145.29	72.55	4.00

microstructural domain. The three-step simulation-characterization-partitioning technique provides a delineation of various length scales in the microstructure.

The second module is for detailed micromechanical analysis of particle fragmentation and matrix cracking of heterogeneous microstructures leading to ductile fracture. This module is necessary for RVE level analysis with periodicity as well

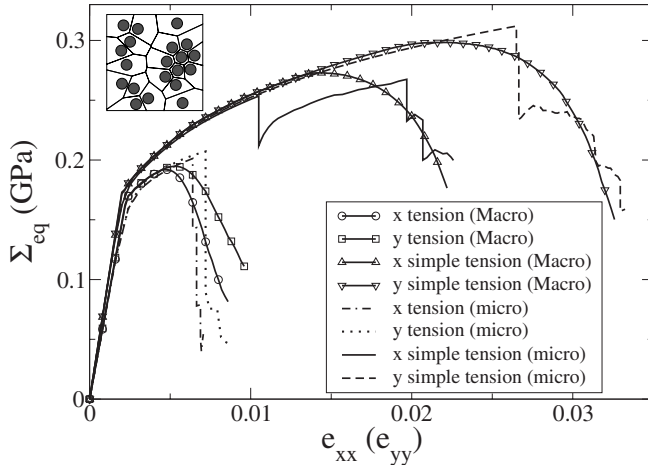


Fig. 21. Comparison of equivalent stress by HAPD model-based macroscopic analysis with micromechanics analysis.

as pure micromechanical analysis in regions where periodicity ceases to hold in the multilevel analysis discussed in Refs. 11 and 12. A locally enriched Voronoi cell FEM or LE-VCFEM is developed for particle fragmentation followed by ductile failure through matrix cracking in the form of void growth and coalescence. A nonlocal Gurson–Tvergaard–Needleman (GTN) model is used to model ductile failure in the matrix. The assumed stress-based hybrid VCFEM formulation is adaptively overlaid with narrow bands of displacement-based elements to accommodate localized strain softening. Numerical examples show the potential of LE-VCFEM in accurate microstructural modeling of ductile fracture.

The third module develops a homogenization-based anisotropic plasticity-damage (HAPD) model for macroscopic analysis in the multiscale modeling framework. The HAPD model is taken to be in the form of the GTN model. Parameters in this model are calibrated from results of homogenization of microstructural variables obtained by LE-VCFEM analysis of microstructural RVE containing particles, matrix and voids. Numerical examples are simulated with this model for different RVEs undergoing a wide variety of load paths. Comparison between the HAPD model and homogenized micromechanic results shows excellent agreement. Thus the model is suitable for being implemented in macroscopic finite element codes to represent ductile failure in composites as long as the basic RVE assumptions remain valid. The authors are currently working on integrating these modules in a comprehensive multiscale framework, which will be reported in subsequent papers.

## Acknowledgments

This work has been supported by the National Science Foundation NSF Div. Civil and Mechanical Systems Division through the GOALI grant no. CMS-0308666

(Program Director: C. Cooper) and by the Department of Energy Aluminum Visions program through grant no. A5997 (subcontract from Univ. of Illinois). This sponsorship is gratefully acknowledged. Computer support by the Ohio Supercomputer Center through grant PAS813-2 is also gratefully acknowledged.

## References

- Q. G. Wang, C. H. Caceres and J. R. Griffiths, Damage by eutectic particle cracking in Aluminum casting alloys A356/357, *Metall. Mater. Trans. A* **34A** (2003) 2901–2912.
- J. M. Boileau, The effect of solidification time on the mechanical properties of a cast 319 aluminum alloy, PhD. dissertation, Wayne State University (2000).
- W. J. Poole and E. J. Dowdle, Experimental measurements of damage evolution in Al–Si eutectic alloys, *Scripta Mater.* **39** (1998) 1281–1287.
- C. H. Caceres, Particle cracking and the tensile ductility of a model Al–Si–Mg composite system, *Aluminum Trans.* **1** (1999) 1–13.
- C. H. Caceres and J. R. Griffiths, Damage by the cracking of silicon particles in an Al-7Si-0.4Mg casting alloy, *Acta Mater.* **44** (1996) 25–33.
- C. Gonzalez and J. Llorca, Prediction of the tensile stress–strain curve and ductility in Al/SiC composites, *Scripta Metall.* **35** (1996) 91–97.
- E. Weissenbek, H. J. Boehm and F. G. Rammerstorfer, Micromechanical investigations of fiber arrangement effects in particle reinforced metal matrix composites, *Comp. Mater. Sci.* **3** (1994) 263–278.
- M. Li, S. Ghosh and O. Richmond, An experimental–computational approach to the investigation of damage evolution in discontinuously reinforced aluminum matrix composites, *Acta Mater.* **47** (1999) 3515–3552.
- S. Ghosh and S. Moorthy, Particle fracture simulation in non-uniform microstructures of metal–matrix composites, *Acta Mater.* **46** (1998) 965–982.
- S. Li and S. Ghosh, Debonding in composite microstructures with morphological variations, *Int. J. Comput. Meth.* **1** (2004) 121–149.
- S. Ghosh, K. Lee and P. Raghavan, A multi-level computational model for multiscale damage analysis in composite and porous materials, *Int. J. Solids Struct.* **38** (2001) 2335–2385.
- S. Ghosh, Adaptive concurrent multi-level model for multi-scale analysis of composite materials including damage, *Multiscale Modeling and Simulation of Composite Materials and Structures*, eds. Y. Kwon, D. H. Allen and R. Talreja (Springer, 2008), pp. 83–164.
- S. Ghosh, D. M. Valiveti, S. H. Harris and J. Boileau, Microstructure characterization based domain partitioning as a pre-processor to multi-scale modeling of cast aluminum alloys, *Model. Simul. Mater. Sci. Eng.* **14** (2006) 1363–1396.
- D. M. Valiveti and S. Ghosh, Domain partitioning of multi-phase materials based on multi-scale characterizations: A preprocessor for multi-scale modeling, *Int. J. Numer. Meth. Eng.* **69** (2007) 1717–1754.
- D. Steglich and W. Brocks, Micromechanical modeling of the behavior of ductile materials including particles, *Comput. Mater. Sci.* **9** (1997) 7–17.
- J. Llorca and C. Gonzalez, Microstructural factors controlling the strength and ductility of particle reinforced metal–matrix composites, *J. Mech. Phys. Solids.* **46** (1998) 1–28.
- V. Tvergaard and A. Needleman, Effect of non-local damage in porous plastic solids, *Int. J. Solids. Struct.* **32** (1995) 1063–1077.

18. V. Tvergaard and A. Needleman, Nonlocal effects on localization in a void-sheet, *Int. J. Solids Struct.* **34** (1997) 2221–2238.
19. W. Y. Chien, J. Pan and S. C. Tang, Modified anisotropic Gurson yield criterion for porous ductile sheet metals, *J. Eng. Mater. Tech.* **123** (2001) 409–416.
20. A. A. Benzaiga, J. Besson and A. Pineau, Anisotropic ductile fracture, part II: Theory, *Acta Mater.* **52** (2004) 4639–4650.
21. A. A. Benzaiga, J. Besson, R. Batisse and A. Pineau, Synergistic effects of plastic anisotropy and void coalescence on fracture mode in plane strain, *Model. Simul. Mater. Sci. Eng.* **10** (2002) 73–102.
22. A. Tewari, A. M. Gokhale, J. E. Spowart and D. B. Miracle, Quantitative characterization of spatial clustering in three-dimensional microstructures using two-point correlation functions, *Acta Mater.* **52** (2004) 307–319.
23. M. D. Rintoul and S. Torquato, Reconstruction of structure of dispersions, *J. Coll. Interf. Sci.* **186** (1997) 467–476.
24. D. W. Cooper, Random sequential packing simulation in three dimensions for spheres, *Phys. Rev. A* **38** (1998) 522–524.
25. R. Everson, L. Sirovich and K. R. Sreenivasan, Wavelet analysis of the turbulent jet, *Physics Letters A* **145** (1990) 314–322.
26. S. Torquato, *Random Heterogeneous Materials: Microstructure and Macroscopic Properties* (Springer-Verlag, New York, 2002).
27. J. E. Spowart, B. Maruyama and D. B. Miracle, Multiscale characterization of spatially heterogeneous systems: Implications for discontinuously reinforced metal-matrix composite microstructures, *Mater. Sci. Eng.* **A307** (2001) 51–66.
28. S. Ghosh and N. Kikuchi, An arbitrary Lagrangian–Eulerian finite element method for large deformation analysis of elastic–viscoplastic solids, *Comput. Meth. Appl. Mech. Eng.* **86** (1991) 127–188.
29. N. Aravas, On the numerical integration of a class of pressure-dependent plasticity models, *Int. J. Numer. Meth. Eng.* **24** (1987) 1395–1416.
30. C. C. Chu and A. Needleman, Void nucleation effects in biaxially stretched sheets, *J. Eng. Mater. Tech.* **102** (1980) 249–256.
31. V. Tvergaard, Influence of voids on shear band instabilities under plane strain conditions, *Int. J. Fract. Mech.* **17** (1981) 389–407.
32. O. C. Zienkiewicz and J. Z. Zhu, The super-convergent patch recovery and a posteriori error estimates. Part 1: The recovery technique, *Int. J. Numer. Meth. Eng.* **33** (1992) 1331–1364.
33. R. A. Hill, A theory of yielding and plastic flow of anisotropic metals, *Proc. Roy. Soc. Lond. Ser. A* **193** (1948) 281–297.
34. D. Wang, J. Pan and S. Liu, An anisotropic Gurson yield criterion for porous ductile sheet metals with planar anisotropy, *Int. J. Damage Mech.* **13** (2004) 7–33.